Journal of Zhejiang University-SCIENCE A 2025 26(12):1258-1272
www.jzus.zju.edu.cn; www.springer.com/journal/11582
E-mail: jzus_a@zju.edu.cn

Research Article
https://doi.org/10.1631/jzus.A2500022

Flow field patterns in train compartments based on jet ventilation under variable air volume system: isothermal conditions

Songbo WU, Tian LI✉, Jiye ZHANG

State Key Laboratory of Rail Transit Vehicle System, Southwest Jiaotong University, Chengdu 610031, China

Abstract: Variable air volume systems are widely used in trains as they provide effective energy savings for air conditioning. However, the design phase is usually carried out at a certain fixed airflow, resulting in a difference between the expected and actual flow fields. In this study, we first analyzed the flow field characteristics at variable airflow rates under isothermal conditions, and subsequently established a correlation equation between the airflow and the flow field parameters. The results show that the airflow just entering the compartment conforms to the characteristics of an attached jet, and then, after converging in the middle, conforms to the characteristics of a free jet. The flow field characteristics are significantly correlated with the Reynolds number (*Re*) and are limited by the small space inside the vehicle. When $Re \geqslant 2650$, the axial velocities all conform to the classical u_m/u_0–$(x/b)^r$ or u_m/u_0–$(y/b)^r$ law, the sectional velocities conform to the exponential and Gaussian distributions, and the characteristic thicknesses of the jets conform to a linear distribution. Derivation shows that the entrainment suction flow rate is related mainly to the initial flow rate and the air opening width. The results of this study will inform the design of ventilation systems for high-speed trains.

Key words: High-speed train; Internal flow field; Ventilation; Numerical simulation

1 Introduction

With the development of urban construction and breakthroughs in key technologies, high-speed trains have become one of the most popular modes of transportation (Tian, 2019; Zhang et al., 2022; Fang and Ma, 2023; Li et al., 2024; Liu et al., 2024; Song et al., 2025). The compartment of a high-speed train is an enclosed space, and passengers are often required to stay in the compartment for several hours. A good thermal comfort and cabin environment during train operation needs to be regulated by an efficient and reliable ventilation system (Li et al., 2019; Woodward et al., 2022; Wang TT et al., 2024a). How to create a healthy and comfortable cabin environment with low energy consumption is one of the key issues facing high-speed train designers. There are at least two challenges: the optimized design of the ventilation structure and the strategy applied under variable air volume (VAV) air conditioning parameters.

Researchers have explored the ventilation systems of high-speed trains (Li et al., 2022; Schmeling et al., 2022; Liu et al., 2023; Yang et al., 2024; Wu et al., 2025; Xu et al., 2026). Lu et al. (2023) applied an improved proper orthogonal decomposition reconstruction method for multi-objective optimization of a high-speed train ventilation system, showing that ventilation parameter optimization significantly boosts air quality. Wang TT et al. (2024b) investigated reducing contaminant diffusion and infection risk in compartments by adjusting intake tract turbulence intensity, achieving an increase in decontamination rate from 0.23 to 1.86. Schmeling and Volkmann (2020) studied the interaction between ventilation methods and cabin thermal comfort, proposing a new low-momentum ventilation scheme. Wu et al. (2024) used experiments and numerical simulations to study formaldehyde distribution in high-speed train compartments, analyzing the link between ventilation parameters and concentration, revealing that ventilation modes/parameters significantly influence its distribution. Chang et al. (2021) proposed a novel hybrid ventilation system based on an original design,

✉ Tian LI, litian2008@home.swjtu.edu.cn
Songbo WU, https://orcid.org/0000-0003-0153-0137
Tian LI, https://orcid.org/0000-0002-7345-7488

Received Jan. 21, 2025; Revision accepted June 3, 2025;
Crosschecked Nov. 23, 2025

demonstrating improved thermal comfort and lower energy consumption. Aliahmadipour et al. (2017) explored summer train compartment flow field characteristics, noting improper design degrades the air environment, while structural improvements for symmetrical airflow enhance thermal comfort. Xu et al. (2022) investigated how different ventilation methods affect compartment flow fields and droplet diffusion, finding that top air supply reduces infection risk and inhibits virus longitudinal spread. Yang et al. (2018) studied the impact of different diffusers on thermal flow and pollutant distribution fields in compartments, showing that thermal plumes may cause pollutant locking. Scholars have also advanced VAV ventilation strategies and design theories. Liu et al. (2011) analyzed dynamic cooling loads in train carriages during summer peak conditions, revealing significant regional and temporal variations. Wang et al. (2020) showed that VAV systems reduce energy consumption by 14.5% compared to fixed-volume systems, while inverter controls save 14.0%–31.5% over on/off operation. Chen et al. (2024) developed an adaptive temperature control model considering air infiltration, thermal comfort, and energy consumption, achieving a 0.069 °C temperature error reduction and 1.534 kWh energy savings per compartment. To address air-conditioning system time lag issues, Bai et al. (2008) proposed an adaptive proportional integral (PI) controller with a Smith predictor, improving control stability. Zhang et al. (2015) introduced a model-free static pressure reset fuzzy control method for nonlinear VAV systems, achieving at least 7% energy savings. Relevant studies have also been conducted in the field of jet ventilation systems (Wang J et al., 2024). Han and Li (2021) investigated the velocity distribution of wall-attached jets in slotted-inlet ventilated spaces under isothermal conditions and derived unified mathematical equations to describe the decay of centerline velocity and the distribution of velocity profiles. Cao et al. (2010) conducted a series of experiments on ceiling-attached jets and their flow characteristics after impinging on a corner. They focused on the jet impingement region and the flow characteristics of the jet after deflection, proposing a virtual origin model for predicting the centerline velocity of the jet after deflection. Triboix and Marchal (2002) performed a stability analysis of the mechanism of jet attachment to walls and presented a formula relating the penetration distance and the height of the slot to the Archimedes number (*Ar*), based on the fundamental assumption of self-similar velocity and temperature profiles. Yu et al. (2003) carried out a scaled model study on the velocity and thermal fields of slotted ventilation ceilings under isothermal conditions, analyzing the airflow patterns, decay of centerline velocity and temperature, and velocity and temperature profiles, and established relevant semi-empirical predictive equations. Yin et al. (2021) studied the application and mechanism of air distribution of column-attached ventilation in winter heating conditions and found that the *Ar* is related to air distribution and ventilation effectiveness. An *Ar* value less than 2.241×10^{-3} is a prerequisite for effective airflow, and the heat transfer efficiency is negatively and linearly correlated with the *Ar* value.

The above research shows that VAV systems can effectively save energy. However, most of these studies have concentrated on ventilation system design under fixed air volume conditions. This focus has left a gap in addressing the dynamic challenges encountered during train operation, such as fluctuations in heat load and external climate conditions. These dynamic factors can lead to mismatches between the fixed air volume design and actual requirements, resulting in either excessive or insufficient cooling/heating capacity. This not only causes unnecessary energy consumption but also compromises passenger thermal comfort. Moreover, current VAV control strategies are largely based on preset static parameters, which severely limit their ability to adapt to the real-time variations in the in-car flow field heat load. To bridge this gap, in the present study, we endeavored to uncover the evolution patterns of the flow field under both isothermal and VAV conditions. By establishing correlation equations between air volume and flow field parameters, we aimed to provide a robust theoretical foundation for the development of intelligent ventilation control systems. This advancement is expected to offer innovative solutions for enhancing thermal comfort while simultaneously achieving energy savings. The findings of this study are expected to hold substantial reference value for the evolution of ventilation systems within the rail transit industry, potentially guiding future advancements towards more efficient and adaptive designs.

2 Turbulence model

The air flow in train compartments is a low-speed turbulent flow, and the flow field information can be

predicted by solving the incompressible Navier-Stokes equations. Realizable k-ε is a classical two-equation model shown to be sufficiently accurate in predicting the flow field in compartments (Cao et al., 2022; Wu et al., 2023). Therefore, this model was used here for flow field prediction with an enhanced wall function for the near-wall surface. The generalized governing equations were as follows:

$$\frac{\partial}{\partial t}(\rho k)+\frac{\partial}{\partial x_j}(\rho k u_j)=\frac{\partial}{\partial x_j}\left[\left(\mu+\frac{\mu_t}{\sigma_k}\right)\frac{\partial k}{\partial x_j}\right]+G_k+G_b-\rho\varepsilon-Y_M+S_k, \tag{1}$$

$$\frac{\partial}{\partial t}(\rho \varepsilon)+\frac{\partial}{\partial x_j}(\rho \varepsilon u_j)=\frac{\partial}{\partial x_j}\left[\left(\mu+\frac{\mu_t}{\sigma_\varepsilon}\right)\frac{\partial \varepsilon}{\partial x_j}\right]+\rho C_1 S\varepsilon-\rho C_2\frac{\varepsilon^2}{k+\sqrt{v\varepsilon}}+C_{1\varepsilon}\frac{\varepsilon}{k}C_{3\varepsilon}G_b+S_\varepsilon, \tag{2}$$

$$C_1=\max\left(0.43,\ \frac{\eta'}{\eta'+5}\right),\ \eta'=S\frac{k}{\varepsilon},\ S=\sqrt{2\boldsymbol{S}_{ij}\boldsymbol{S}_{ij}}, \tag{3}$$

where t is the physic time; ρ is the air density; u_j is the air velocity (component in the jth direction); x_j is the spatial position (component in the jth direction); μ is the dynamic viscosity of the fluid; v is the kinematic viscosity of the fluid; μ_t is the turbulent dynamic viscosity; $\boldsymbol{S}_{ij}$ is the strain-rate tensor; S is the magnitude of the strain-rate tensor; η' is the dimensionless parameter used in the turbulence model to determine the coefficient C_1; G_b and G_k are the generations of turbulent kinetic energy due to buoyancy and the mean velocity gradients, respectively; Y_M represents the contribution of fluctuating dilatation incompressible turbulence to the overall dissipation rate; k and ε are the turbulent kinetic energy and turbulent dissipation rate, respectively; σ_k and σ_ε are the turbulent Prandtl numbers for k and ε, respectively; C_2, $C_{1\varepsilon}$, and $C_{3\varepsilon}$ are constants; S_k and S_ε are user-defined source terms.

3 Computational model

3.1 Numerical model

A full-size geometric model was developed based on the carriages of a high-speed train that is in service. The length, width, and height of the carriages are about 18300 mm, 3200 mm, and 2300 mm, respectively. The occupants of a car in fully loaded condition total 90, with a 3+2 seating distribution. The air intake of the cabin is located on both sides of the ceiling, and the exhaust is located on both sides of the floor (Fig. 1).

The cases for the isothermal jet are given in Table 1. When calculating the Reynolds number (Re), the characteristic length is taken as the slit width of the air supply opening, which is specifically b=20 mm. To reveal the effect of different Re values on the jet law, several sets of small and large airflow conditions were also selected. During the calculations, all working conditions were set to an isothermal mode with a temperature difference (ΔT) of 0 °C; the ventilation flow rate (Q) ranged from 6 to 20 L/(s·person), corresponding to Re approximately between 990 and 3310, and the corresponding initial air supply velocity (u_0) ranged from about 0.735 to 2.449 m/s.

3.2 Boundary conditions

The carriages of high-speed trains are relatively closed, and the indoor environment is uniformly regulated by the air-conditioning system. The airflow in the

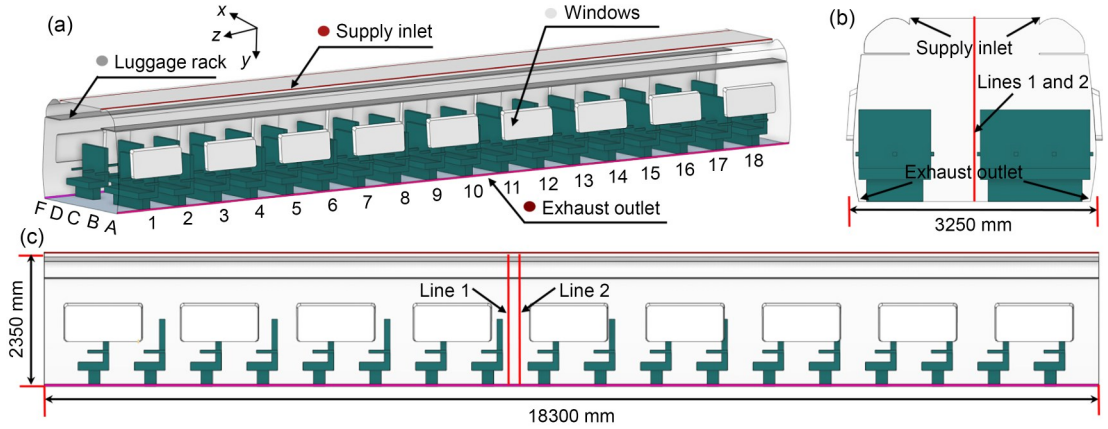

Fig. 1 Geometric model of the train carriage

Table 1 Cases for the isothermal jet (b=20 mm)

Case	Q (L/(s·person))	ΔT (°C)	u_0 (m/s)	Re
1	6	0	0.735	990
2	8	0	0.980	1330
3	10	0	1.225	1660
4	12	0	1.470	1990
5	14	0	1.714	2320
6	16	0	1.960	2650
7	18	0	2.204	2980
8	20	0	2.449	3310

compartment is small and incompressible, and its material properties are considered to be incompressible ideal gases. Here, we assumed that the air flow was fully mixed and uniformly distributed before entering the passenger compartment. Therefore, the boundary condition of the air supply outlet was set as a velocity-inlet, and the magnitude of the velocity was a fixed value (Lu et al., 2023). The air supply temperature of the air conditioner was set at 22 °C, and the flow rate was determined by the specific calculation conditions. Since the distribution of the specific flow parameters at the air exhaust outlet is complex and difficult to determine, the boundary condition was set as an outflow. This method can automatically adjust the state at the outlet according to the internal flow situation. During the operation of the train, the flow field inside the car will be affected by the solar thermal radiation and the heat conduction of the car body. Here, we assumed that the ambient temperature was 35 °C and the solar radiation intensity 800 W/m^2 (Li et al., 2022; Xu et al., 2022). Considering the differences in structural design, material properties, and processing techniques, the heat transfer coefficients of the side walls, floor, end walls, and windows were set to 0.9, 1.2, 1.2, and 1.4 W/(m^2·K), respectively (Wu et al., 2023).

In the solution of the Navier-Stokes equations, the realizable k-ε turbulence model was selected, and enhanced wall functions were used to handle the near-wall region. The semi-implicit method for pressure-linked equations (SIMPLE) algorithm was chosen to solve the pressure–velocity coupling terms. The least-squares cell-based method was selected for calculating the physical quantity gradients on the grid cells. The pressure staggering option (PRESTO!) discretization scheme was adopted for pressure, and second-order upwind discretization schemes were used for turbulent kinetic energy, turbulent dissipation rate, momentum, and energy.

3.3 Mesh independence

To ensure that the computational results were not affected by the numerical grids, grid independence verification was first needed. The numerical grid division of the carriage model was carried out using Fluent Meshing software, with the Poly grid type. Three sets of grids with different scales were divided, and the number of body grids was about 6.8, 21.7, and 34.5 million, respectively. The maximum size of the body grid corresponded to 36, 28, and 20 mm, respectively. To ensure that y^+ was less than 3 in most regions, a two-layer boundary layer was delineated, with the height of the first boundary layer being 2 mm. Fig. 2 presents the computational results from the three grid sets. It shows the air velocity (u) profiles along two sampling lines, the locations of which are specified in Fig. 1. Calculation results showed that the change rule of each physical quantity was consistent and showed a small deviation when using medium or fine grids. Considering the calculation accuracy and calculation speed, the medium grid was used here for calculation. The specific dimensions were: the surface grid sizes of the air supply and exhaust vents were 2 mm and 5 mm, respectively; the surface grid size of the seats and the train was 24 mm; the maximum size of the body grid was 28 mm. Fig. 3 shows a schematic diagram of the grid. Details of the verification of numerical methods are given in Section S1 of the electronic supplementary materials (ESM).

4 Results

First, we analyzed the interrelationship between VAV ventilation and flow field characteristics under isothermal conditions. Subsequently, we established the correlation equation for the interaction between the VAV and the flow field parameters in the vehicle by combining the Prandtl turbulence hypothesis and some classical theories.

4.1 Air flow characteristics

4.1.1 Distribution of velocity field

Fig. 4 illustrates the velocity field distribution under different Re values. When the jet flow enters the compartment, it immediately adheres to the ceiling surface

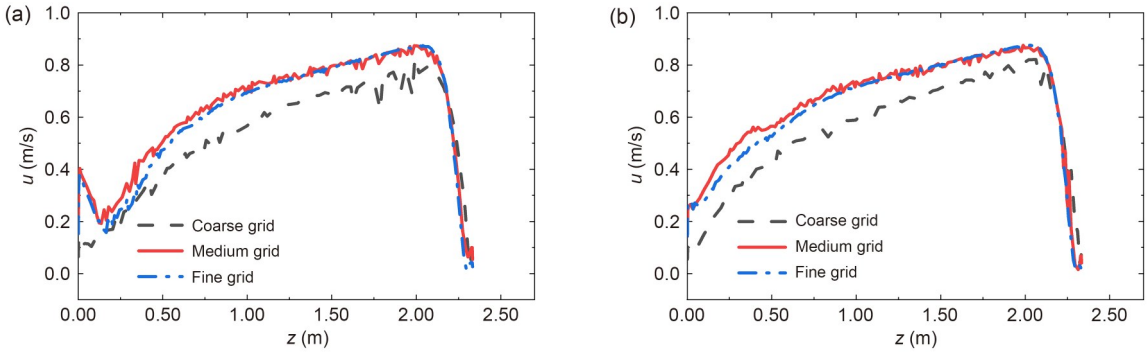

Fig. 2 Grid independence test: (a) line 1; (b) line 2

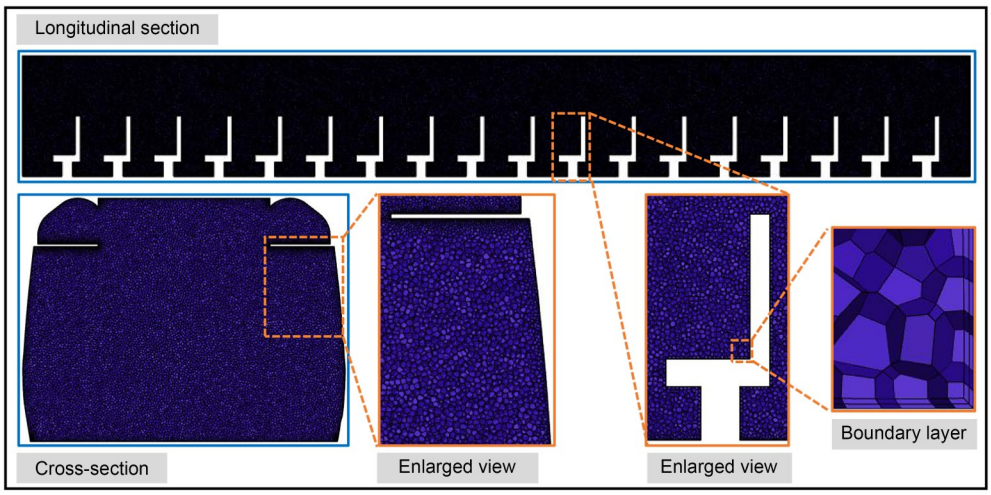

Fig. 3 Mesh generation

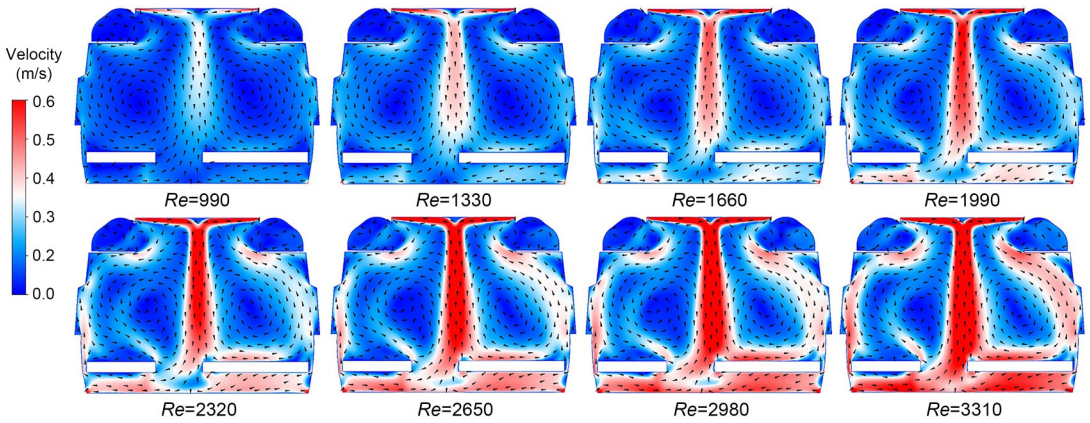

Fig. 4 Time-averaged velocity vector fields at different Reynolds numbers

due to the Coanda effect, a phenomenon where fluid flow tends to attach to a nearby surface, presenting characteristics typical of an adherent jet. After converging at the mid-ceiling position, the airflow begins to diffuse downward, exhibiting features of a free jet. In this free jet stage, the airflow is no longer restricted by surface attachment, enabling unrestricted spreading. Driven by the two jet flow volumes, part of the airflow forms a large-scale airflow circulation in the passenger area. The velocity field distribution is significantly influenced by the *Re* (Fig. 4). Quantitatively, there is a positive correlation between the overall airflow velocity in the vehicle

and the *Re*, meaning the airflow velocity increases as the *Re* rises. Notably, across all six *Re* values investigated, a fixed pattern of fully circulating airflow is generated in the compartment. Although the velocity field allows for qualitative analysis of the flow field (e.g., observing flow patterns and circulation structures), quantitative analysis remains essential. This is because quantitative methods can reveal intrinsic properties of the compartment's flow field, such as precise velocity magnitude distributions, circulation intensity metrics, and dynamic flow characteristics that cannot be fully captured through qualitative observation alone.

Note that two right-angle coordinate systems are involved in the flow field analysis, x–y and x^*–y, with the z-axis perpendicular to the cross-section. The coordinate origin is located at the outlet of the air supply when analyzing the attached jet (Fig. 5a) and in the middle of the top of the compartment when analyzing the free jet (Fig. 5b). Four monitoring lines were established along the x-direction and six in the y-direction to monitor the velocity profile of the flow field in the compartment (Fig. 5). The four positions along the x-direction were 150, 300, 450, and 600 mm. The six positions along the y-direction were 300, 600, 900, 1200, 1500, and 1800 mm.

Fig. 6 illustrates the velocity profiles at four positions along the x-direction. For comparison, the velocity profiles are dimensionless using the axial velocity

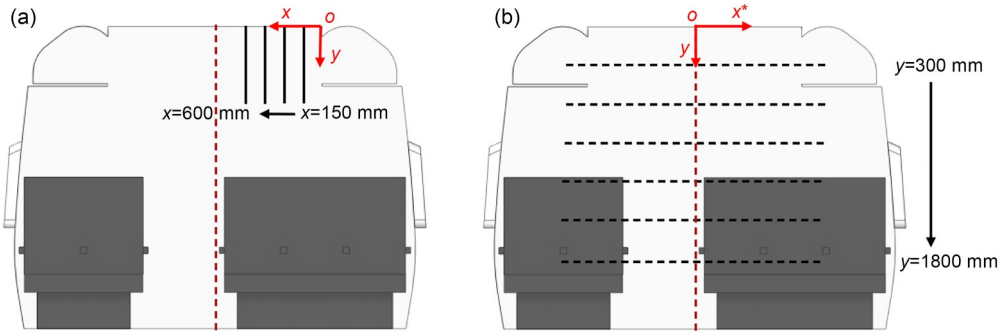

Fig. 5 Schematic diagram of the location of the monitoring lines in the compartment

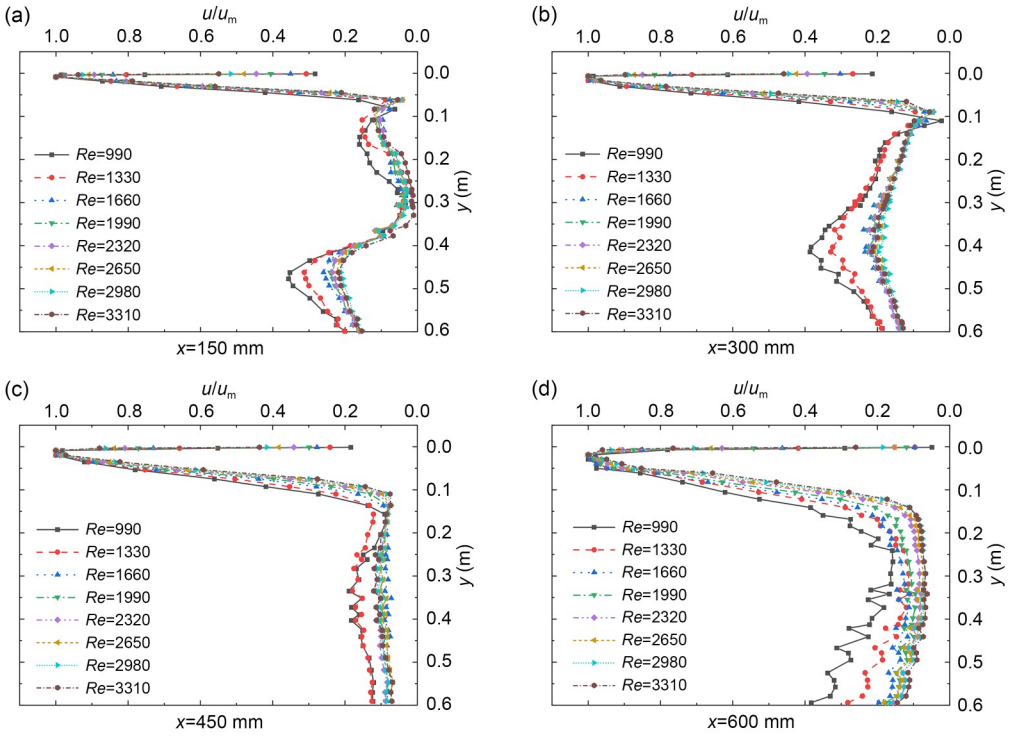

Fig. 6 Cross-sectional velocity distribution in the attached jet region: (a) x=150 mm; (b) x=300 mm; (c) x=450 mm; (d) x=600 mm

(u_m) of the location, and the dimensionless parameter is u/u_m. The location of the maximum axial velocity at the same position for different *Re* values is essentially certain. After the jets are ejected from the slit, they all show the characteristics of attached jets. In the inner layers of the attached jets, the dimensionless velocity profiles essentially overlap, exhibiting Reynolds independence. In the outer layer of the attached jet, the jet thickness decreases as the *Re* increases, and the dimensionless velocity (u/u_m) at the same location is smaller. Below the main region of the jet, the dimensionless velocities at low *Re* values ($Re\leqslant1330$) are larger and more capable of inducing cyclonic rise in the flow. It may be that the dominant vortex structure within the shear layer at low *Re* values is larger, and its relative entrainment and sucking capacity is stronger and more capable of promoting the development of the jet. This is in general agreement with the findings of Suresh et al. (2008) and Cao et al. (2014). As the distance from the jet outlet position increases, the thickness of the jet also gradually increases, and the ability to coil and suck the airflow gradually increases. However, this difference decreases with increasing *Re* values, and the velocity profiles at high *Re* values ($Re\geqslant2320$) gradually show Reynolds independence.

Fig. 7 illustrates the dimensionless velocity profiles at the six positions along the *y*-direction. Similarly, the locations of the maximum axial velocities at different *Re* values are essentially the same and are located in the mid-section region of the compartment (x^*=0 m). The velocity development pattern in the middle of the compartment exhibits some free jet characteristics, but its development pattern can be equally limited by the space of the compartment. Two sets of vortex structures are formed on both sides of the free jet under the dual effect of jet entrainment and compartment micro space. As the jet progresses downward, the thickness of the jet gradually increases. In contrast, the region outside the main jet is significantly affected by the vortex structure. At the same location, the thickness and dimensionless

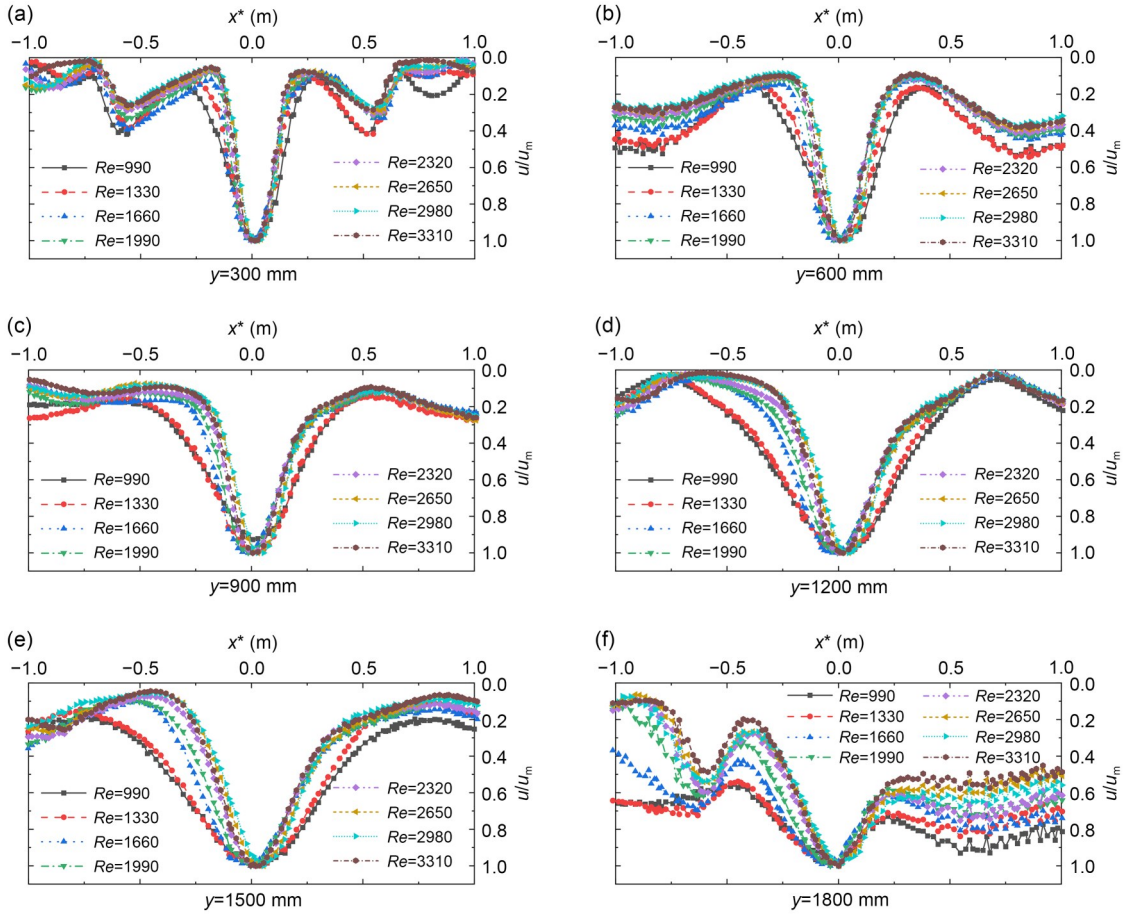

Fig. 7 Cross-sectional velocity distribution in the free jet region: (a) *y*=300 mm; (b) *y*=600 mm; (c) *y*=900 mm; (d) *y*=1200 mm; (e) *y*=1500 mm; (f) *y*=1800 mm

velocity of the jet at low *Re* values (*Re*≤1330) are larger, which suggests that it is more efficient in entrainment of the surrounding air. As the *Re* increases, the thickness of the jet gradually increases, but the rate of change of the increase decreases, and the velocity profiles at high *Re* values largely overlap. Note that when y= 1800 mm, the velocity profile law is affected differently by the asymmetric seat.

4.1.2 Distribution of vorticity field

As the jet develops, it constantly entrains and sucks in the surrounding gases and creates a vortex structure. These vortex structures play an important role in the development of the jet and the distribution of the flow field. Fig. 8 shows the time-averaged vorticity field distribution at different *Re* values. The positivity and negativity of the vorticity field give a clear picture of the rotational direction of the flow as well as the shear and boundary layers of the attached jet. For the attached and free jet regions, the line of intersection between the two is the center axis of the jet. For adherent jets, the centerline gradually bends downward. For free jets, the centerline is essentially located in the middle of the compartment. As the *Re* increases, the strength of the vortex structure gradually increases. This indicates that the jet entrainment capacity is also increasing and is capable of suctioning more surrounding air, which is conducive to improving the ventilation efficiency of the system.

The main drivers behind the continuous development and expansion of the jet are the guidance and entrainment of the external airflow via the entrainment effect, which in turn gives rise to a vortex structure. To analyze the similarity in vorticity across different *Re* values and nullify the impact of units, we rendered the vorticity dimensionless. Its definition was as follows:

$$w'=w\times\frac{b}{u_0}=\left(\frac{\partial u_z}{\partial y}-\frac{\partial u_y}{\partial z}\right)\frac{b}{u_0}, \tag{4}$$

where w represents the vorticity, w' represents the dimensionless spanwise vorticity, and u_y and u_z denote the velocity scalars of the airflow in the y-direction and z-direction, respectively.

Fig. 9 illustrates the dimensionless vorticity distribution within the attached jet region. When *Re*≥990, a consistent pattern emerges in the vorticity distribution. Near the wall boundary layer, the vorticity is positive and relatively high, but it swiftly diminishes to zero. This transition point marks the interface between the boundary layer and the shear layer, and this change occurs very abruptly. Following this, the vorticity surges sharply in the positive direction, reaching a peak value before gradually subsiding. Overall, the vorticity is notably higher in the inner jet region, which signifies a stronger vortex structure and enhanced entrainment capability. Conversely, in the outer jet region, the vorticity is relatively low and continues to decrease with increasing distance (y). When x≥300 mm and the jet has fully developed into the main flow region, the vorticity approaches zero. Additionally, as the entrainment flow increases and the jet momentum diminishes, the vorticity also progressively decreases with increasing distance x. This trend indicates that both the strength of the vortex structure and the entrainment ability of the jet weaken as the jet develops from the inner to the outer regions and from the near to the far field. Moreover, the dimensionless vorticity increases with a higher *Re*, suggesting

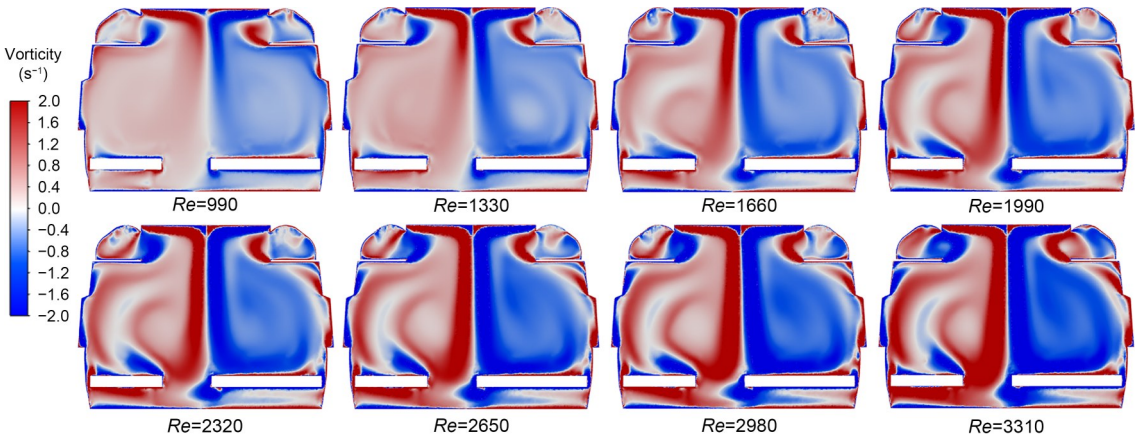

Fig. 8 Time-averaged vortex fields at different Reynolds numbers

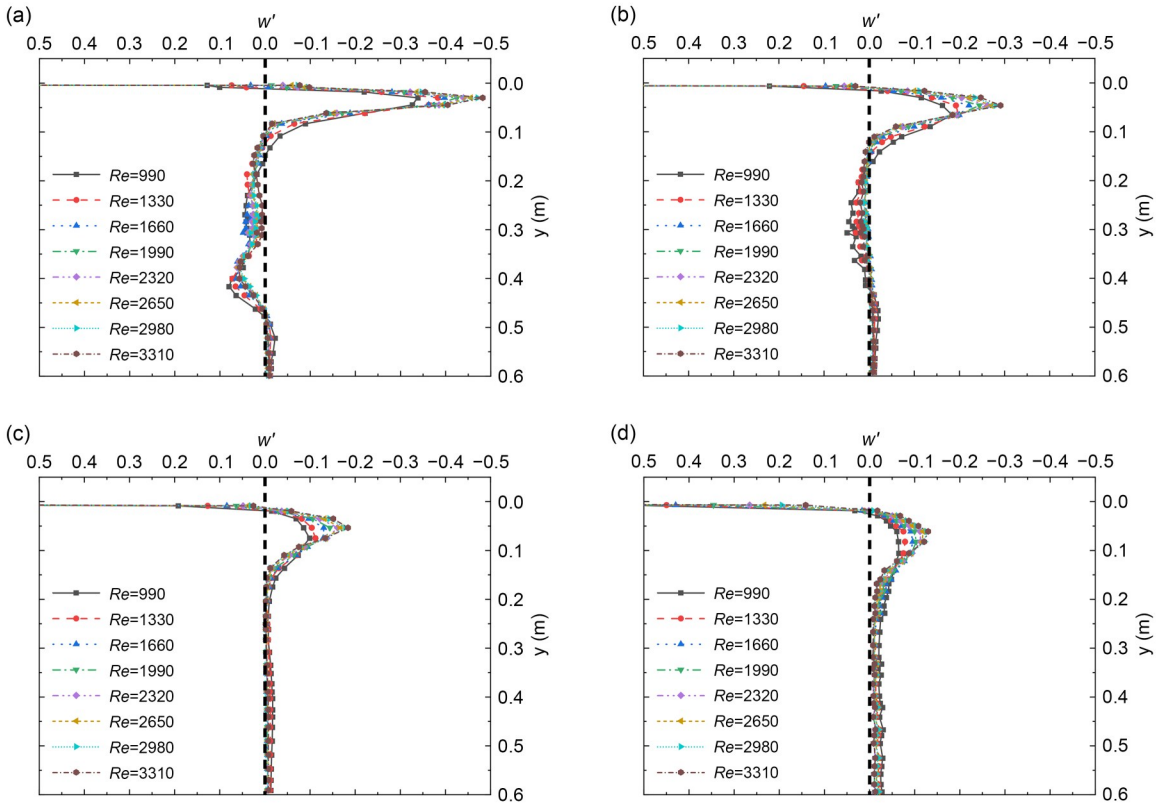

Fig. 9 Dimensionless vorticity profiles in the region of the attached jet: (a) x=150 mm; (b) x=300 mm; (c) x=450 mm; (d) x=600 mm

improved entrainment efficiency per unit flow. However, note that the gradient of this increase diminishes with rising *Re* and eventually becomes independent of the *Re*.

4.2 "Parameter–flow field" theoretical calculation

From the flow field analysis, the air flow entering the carriage undergoes two stages successively: attached jet flow (region I) and free jet flow (region II). Details are given in Section S2 of the ESM. In this section, we describe the "parameter–field" theoretical calculation for the attached and free jet regions under isothermal conditions, including the axial velocity distribution law, the section velocity distribution law, the characteristic thickness of the jet, and the jet entrainment volume.

4.2.1 Distribution of jet axial velocity

Based on extensive experimental observations, in the longitudinal expansion of turbulent jets, both the longitudinal time-averaged velocity and axial velocity gradually decay. Due to the similarity of the time-averaged velocity in the main body section of the jet, combined with the coordinate system in Fig. 5, the axial velocity distribution in the attached jet region can be set as $f(u_m/u_0, x/b)=0$, and in the free jet region as $f(u_m/u_0, y/b)=0$.

Relevant studies have derived the distribution law of jet axial velocity (Li, 2020). Details are given in Section S3 of the ESM. The derivation of the above equations is based on multiple assumptions and experimental parameters from simplified models, such as Prandtl's new turbulence hypothesis and the similarity of turbulent shear stress. However, jet ventilation in train carriages is constrained by more complex geometric spaces and air outlet types. Therefore, certain discrepancies exist, and based on the derivation, it can be assumed that:

$$\frac{u_0}{u_m} \sim \left(\frac{x}{b}\right)^r, \quad r>0, \tag{5}$$

where r can be determined by experiments and reflects the momentum decay rate of the jet.

The law of variation of dimensionless velocity (u_m/u_0) along the axis is given in Fig. 10. Fig. 10a shows the axial velocity in the region of the attached jet and Fig. 10b the axial velocity in the region of the free jet. Theoretical calculations of incompressible flows for turbulent boundary layers have not developed enough to allow a move away from semi-empirical theories. Here, we attempt to establish a semi-empirical formula for the axial velocity of train ventilation in conjunction with the theoretical analysis of the Prandtl turbulence hypothesis. In the region of attached jets, the decay rate of dimensionless axial velocities increases with decreasing *Re*. As a result, the axial velocities at low *Re* values are relatively small in the trailing region of the free jet, which also leads to relatively small initial velocities in the free jet region. When $Re\geqslant 2650$, the decay rates of the attached jets are basically the same. Therefore, for jets with $Re\geqslant 2650$, the decay law of the jet axial velocity before reaching the collision zone ($x/b\leqslant 32.5$) can be described uniformly as:

$$\frac{u_m}{u_0}=\frac{1}{0.007(x/b)^{1.46}+1}. \tag{6}$$

In the free jet region, the jet decay rate is essentially the same, with the jet decaying relatively slowly. When $y/b=15$, at u_m/u_0 between 0.35 and 0.45, and when $y/b=95$, at u_m/u_0 near 0.25, after fitting, it is found that for jets with $Re\geqslant 2650$, the decay law of the jet axial velocity in the free jet range ($15\leqslant y/b\leqslant 95$) can be described uniformly as:

$$\frac{u_m}{u_0}=\frac{0.446}{3.37\times 10^{-8}(y/b)^{3.7}+1}. \tag{7}$$

4.2.2 Distribution of section velocity

For an attached jet air supply, according to the classical theoretical studies of Glauert (1956), Schwarz and Cosart (1961), and Verhoff (1963), the velocities within the jet zone conform to an exponential form of distribution and show similarity in the velocities at different cross-sections. The theoretical velocity profile in the laminar state is given by the Glauert tabulation. The theoretical velocity profiles in the turbulent state are given by the theories of Schwarz and Cosart (1961) and Verhoff (1963), respectively, as follows:

$$\frac{u}{u_m}=\exp\left[-0.973(y/\delta_{0.5}-0.14)^2\right], \tag{8}$$

$$\frac{u}{u_m}=1.48(y/\delta_{0.5})^{1/7}[1-\mathrm{erf}(0.68y/\delta_{0.5})], \tag{9}$$

where exp is the exponential function, erf is the error function, and $\delta_{0.5}$ is the jet characteristic thickness.

Four jet profiles were selected for comparative analysis: for x=150 mm, x=300 mm, x=450 mm, and x=600 mm. Fig. 11 shows that within the main jet zone ($0\leqslant\eta\leqslant 2$), the section velocities are in good agreement with the classical theory. Within the near-wall zone, the velocity increases rapidly from the wall and reaches a maximum value at about η=0.25. In the interval $0.25\leqslant\eta\leqslant 2$, the section velocity begins to decrease gradually until the outer edge of the jet converges with the ambient velocity. Outside the main jet region ($\eta>2$), the velocity is gradually influenced by the surrounding flow field. When $Re\geqslant 1660$, the flow field outside the main flow zone also has high similarity. When the vortex structure exists outside the mainstream region, the velocity distribution is significantly affected by the vortex.

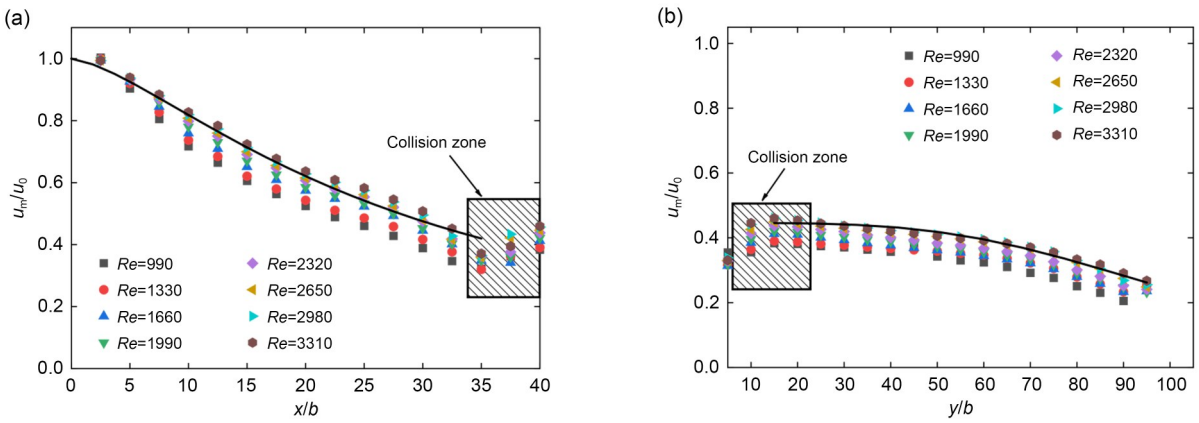

Fig. 10 Jet axial velocity distribution at different Reynolds numbers: (a) attached jet region; (b) free jet region

From experimental study and theoretical analysis, it shows that free turbulent jets are characterized by the similarity of the velocity distribution in the cross-section and linear expansion of the jet boundary (Liu, 2008). In addition, during the jet flow, the velocity distribution of the jet section is characterized by a Gaussian distribution due to vortex pairing and entrainment. Solved according to the classical theory of Tollmien, the section velocity solution for a free jet can be described by (Liu, 2008):

$$\frac{u}{u_{\mathrm{m}}}=\left(0.86+\frac{0.14}{1+|x^{*}/\delta_{0.5}|}\right)\exp\left[-0.621\left(x^{*}/\delta_{0.5}\right)^{2}\right]. \quad (10)$$

Two jet profiles were selected for comparative analysis, taken from a height of 1700 mm (y=600 mm) and 1100 mm (y=1200 mm) from the floor. Fig. 12 shows that the velocity distribution is consistent with the Gaussian distribution in the main jet region ($-2\leqslant\eta\leqslant2$). Considering that the jet axis may be shifted, its center is not necessarily at x^{*}=0 mm. Especially at y=1200 mm, it may be affected mainly by the distribution of seats.

4.2.3 Jet characteristic thickness

As mentioned above, the jet characteristic thickness (jet boundary) increases linearly. According to our data fitting, the characteristic thickness of the jet at different *Re* values also conforms to the law of linear growth, which is consistent with the theoretical derivation.

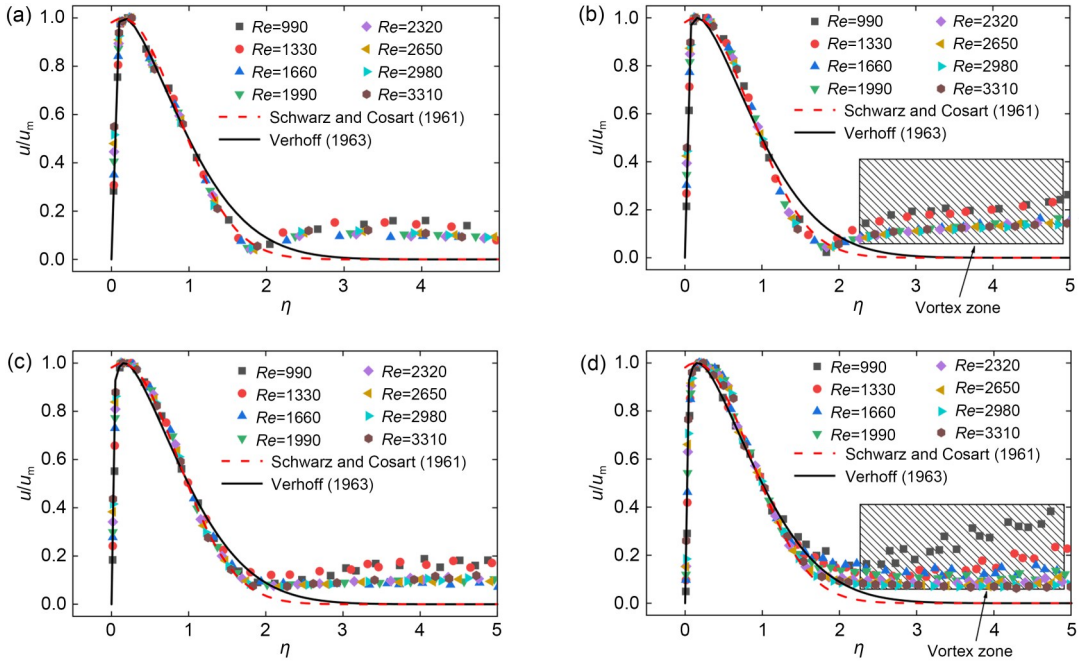

Fig. 11 Section velocity distribution of an attached jet at different Reynolds numbers ($\eta=y/\delta_{0.5}$): (a) x=150 mm; (b) x=300 mm; (c) x=450 mm; (d) x=600 mm

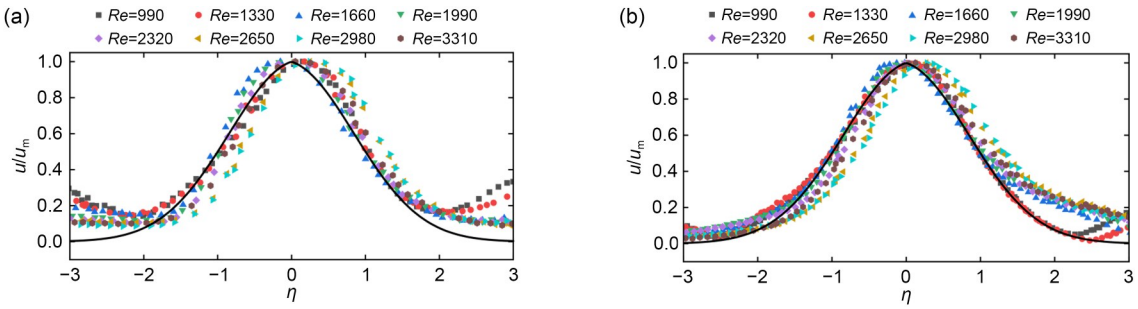

Fig. 12 Section velocity distribution of a free jet at different Reynolds numbers ($\eta=x^{*}/\delta_{0.5}$): (a) y=600 mm; (b) y=1200 mm

Fig. 13 shows that the growth rate of the jet characteristic thickness is related to the *Re*. The growth rates were about 0.15, 0.13, 0.12, 0.11, 0.11, 0.10, 0.10, and 0.10 in the attached jet region and 0.21, 0.20, 0.13, 0.11, 0.10, 0.10, 0.09, and 0.09 in the free jet region. The growth rate decreases with the increase of *Re*, and when *Re*≥2650, it is basically independent of the *Re*. The corresponding functional expressions for the attached jet region and free jet region are described respectively as:

$$\delta_{0.5}=0.1(x-0.05)+0.9b, \tag{11}$$

$$\delta_{0.5}=0.09(y-0.3)+4.4b. \tag{12}$$

4.2.4 Entrainment flow volume of the section

The jet entrainment flow volume Q_a can be calculated by integrating the section as:

$$Q_a=\int_0^{\infty}u\mathrm{d}x. \tag{13}$$

When *Re*≥2650, for attached jets, bringing in the section velocity distribution (Eq. (9)) yields:

$$Q_a=u_m\delta_{0.5}\int_0^{\infty}1.48\eta^{1/7}[1-\mathrm{erf}(0.68\eta)]\mathrm{d}\eta=1.093u_m\delta_{0.5}. \tag{14}$$

Bringing in the axial velocity distribution (Eq. (6)) and the jet characteristic thickness (Eq. (11)) yields:

$$Q_a=u_0\frac{0.109(x+9b-0.05)}{0.007(x/b)^{1.46}+1}. \tag{15}$$

The initial flow rate of the jet is:

$$Q_0=u_0b. \tag{16}$$

The dimensionless equation is obtained by bringing Eq. (16) into Eq. (15):

$$\frac{Q_a}{Q_0}=\frac{0.109(x+9b-0.05)}{b[0.007(x/b)^{1.46}+1]}, \tag{17}$$

where Q_a is the entrainment flow volume of any cross-section of the attached jet, in m^3/s, and Q_0 is the jet initial air supply flow, in m^3/s.

When *Re*≥2650, for a free jet, bringing in the section velocity distribution (Eq. (10)) yields:

$$Q_f=\int_{-\infty}^{\infty}u\mathrm{d}y=2\int_0^{\infty}u\mathrm{d}y=2u_m\delta_{0.5}\times\int_0^{\infty}\left[\left(0.86+\frac{0.14}{1+\eta}\right)\exp(-0.621\eta^2)\right]\mathrm{d}\eta=2.134u_m\delta_{0.5}, \tag{18}$$

where Q_f is the entrainment flow volume of any cross-section of the free jet, in m^3/s.

Bringing in the axial velocity distribution (Eq. (7)) and the jet characteristic thickness (Eq. (12)) yields:

$$Q_f=u_0\frac{0.086(y+48.9b-0.3)}{3.37\times10^{-8}(y/b)^{3.7}+1}. \tag{19}$$

The dimensionless equation is obtained by bringing Eq. (16) into Eq. (19):

$$\frac{Q_f}{Q_0}=\frac{0.086(y+48.9b-0.3)}{b\left[3.37\times10^{-8}(y/b)^{3.7}+1\right]}. \tag{20}$$

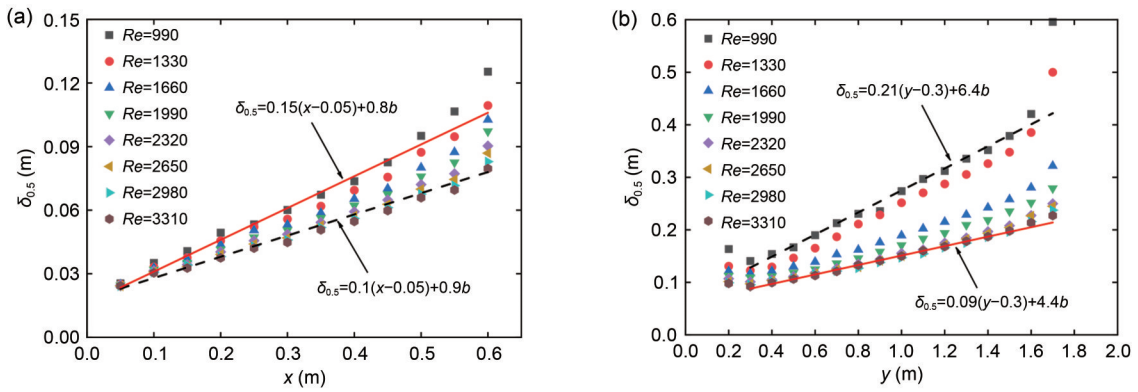

Fig. 13 Characteristic thicknesses of the jet at different Reynolds numbers: (a) attached jet region; (b) free jet region

5 Discussion

This research has achieved notable advancements in elucidating the flow field characteristics of high-speed train carriages operating under VAV systems. However, several limitations and shortcomings are acknowledged (detailed in Section S4 of the ESM).

6 Conclusions

VAV systems are usually used in train operation. To be more in line with the actual operating conditions, the flow field characteristics in train compartments under a VAV system were investigated based on isothermal conditions. Subsequently, the relevant equations for the interaction between the variable airflow and the flow field parameters in the train carriage were revealed by combining the Prandtl turbulence hypothesis and some classical theories. The main conclusions drawn are as follows:

(1) Influenced by the Coanda effect, the jet enters the compartment and attaches to the ceiling, which is consistent with the characteristics of an attached jet. The two sides of the jet converge and then spread downward, in a manner consistent with the characteristics of a free jet. However, the jet state cannot be fully developed due to the tiny environment of the compartment. Two vortices are formed in the compartment by the jet's entrainment effect.

(2) The isothermal jet development trajectories, velocity profiles, and in-vehicle flow field characteristics all exhibit significant *Re* correlations. A dimensionless treatment of the characteristic parameters of the flow field revealed that the flow characteristics are progressively independent of the *Re* when $Re \geqslant 2650$. Flow field characterization parameters and ventilation parameters can be predicted by combining data and classical theory with fitting.

(3) When $Re \geqslant 2650$, the axial velocity conforms to the classical $u_m/u_0-(x/b)^r$ or $u_m/u_0-(y/b)^r$ law; the section velocity conforms to the exponential and Gaussian distributions in classical theory; the jet characteristic thicknesses all conform to a linear distribution.

(4) Through derivation, we found that the jet's entrainment capacity is related to the initial flow rate and the width of the air opening. Improvement of the jet's entrainment capacity is conducive to the improvement of the ventilation efficiency of the system.

In conclusion, this study contributes to a comprehensive explanation and prediction of flow field characteristics under VAV systems. It can also provide fast post-prediction data feedback for real-time regulation of VAV systems, which has potential for improving thermal comfort and energy saving. Therefore, it is of great significance for the design of air conditioning and ventilation in the railroad industry.

Acknowledgments

This work is supported by the National Natural Science Foundation of China (No. 12372049) and the Independent Project of State Key Laboratory of Rail Transit Vehicle System (No. 2025RVL-QY-T24), China.

Author contributions

Songbo WU: investigation, writing–original draft, and methodology. Tian LI: conceptualization, funding acquisition, and writing–review & editing. Jiye ZHANG: resources and funding acquisition.

Conflict of interest

Songbo WU, Tian LI, and Jiye ZHANG declare that they have no conflict of interest.

References

Aliahmadipour M, Abdolzadeh M, Lari K, 2017. Air flow simulation of HVAC system in compartment of a passenger coach. *Applied Thermal Engineering*, 123:973-990. https://doi.org/10.1016/j.applthermaleng.2017.05.086

Bai JB, Wang SW, Zhang XS, 2008. Development of an adaptive Smith predictor-based self-tuning PI controller for an HVAC system in a test room. *Energy and Buildings*, 40(12):2244-2252. https://doi.org/10.1016/j.enbuild.2008.07.002

Cao GY, Ruponen M, Kurnitski J, 2010. Experimental investigation of the velocity distribution of the attached plane jet after impingement with the corner in a high room. *Energy and Buildings*, 42(6):935-944. https://doi.org/10.1016/j.enbuild.2010.01.005

Cao Q, Liu MX, Li XY, et al., 2022. Influencing factors in the simulation of airflow and particle transportation in aircraft cabins by CFD. *Building and Environment*, 207:108413. https://doi.org/10.1016/j.buildenv.2021.108413

Cao XD, Liu JJ, Pei JJ, et al., 2014. 2D-PIV measurement of aircraft cabin air distribution with a high spatial resolution. *Building and Environment*, 82:9-19. https://doi.org/10.1016/j.buildenv.2014.07.027

Chang ZY, Yi K, Liu WW, 2021. A new ventilation mode of air conditioning in subway vehicles and its air distribution performance. *Energy and Built Environment*, 2(1):94-104. https://doi.org/10.1016/j.enbenv.2020.06.005

Chen CJ, Zheng Q, Yang L, 2024. Adaptive iterative learning control of internal temperature for high-speed trains. *Journal*

of Mechanical Science and Technology, 38(1):463-473. https://doi.org/10.1007/s12206-023-1238-3

Fang YT, Ma JE, 2023. High-speed railway transport technology. *Journal of Zhejiang University-SCIENCE A*, 24(3):173-176. https://doi.org/10.1631/jzus.A230HSRT

Glauert MB, 1956. The wall jet. *Journal of Fluid Mechanics*, 1(6):625-643. https://doi.org/10.1017/S002211205600041X

Han O, Li AG, 2021. Velocity distribution of wall-attached jets in slotted-inlet ventilated rooms. *Building and Environment*, 194:107708. https://doi.org/10.1016/j.buildenv.2021.107708

Li AG, 2020. Attachment Ventilation Theory and Design. China Architecture & Building Press, Beijing, China (in Chinese).

Li N, Yang L, Li XD, et al., 2019. Multi-objective optimization for designing of high-speed train cabin ventilation system using particle swarm optimization and multi-fidelity Kriging. *Building and Environment*, 155:161-174. https://doi.org/10.1016/j.buildenv.2019.03.021

Li NX, Li T, Dai ZY, et al., 2024. Effect of streamlined nose length on aerodynamic performance of high-speed train with a speed of 400 km/h. *Journal of Zhejiang University-SCIENCE A*, 25(7):525-540. https://doi.org/10.1631/jzus.A2300301

Li T, Wu SB, Yi C, et al., 2022. Diffusion characteristics and risk assessment of respiratory pollutants in high-speed train carriages. *Journal of Wind Engineering and Industrial Aerodynamics*, 222:104930. https://doi.org/10.1016/j.jweia.2022.104930

Liu N, Wu X, Deng E, et al., 2023. Dust diffusion laws during partition excavation by boom-type roadheader in a metro tunnel. *Tunnelling and Underground Space Technology*, 141:105382. https://doi.org/10.1016/j.tust.2023.105382

Liu PQ, 2008. The Theory of Free Turbulent Jets. Beihang University Press, Beijing, China (in Chinese).

Liu WW, Deng QH, Huang WJ, et al., 2011. Variation in cooling load of a moving air-conditioned train compartment under the effects of ambient conditions and body thermal storage. *Applied Thermal Engineering*, 31(6-7):1150-1162. https://doi.org/10.1016/j.applthermaleng.2010.12.010

Liu YK, Yang WC, Deng E, et al., 2024. Using three turbulence simulation methods for modeling the flying of high-speed railway tunnel lining blocks under piston airflow. *Advances in Wind Engineering*, 1(2):100010. https://doi.org/10.1016/j.awe.2024.100010

Lu YB, Wang TT, Zhao CL, et al., 2023. An efficient design method of indoor ventilation parameters for high-speed trains using improved proper orthogonal decomposition reconstruction. *Journal of Building Engineering*, 71:106600. https://doi.org/10.1016/j.jobe.2023.106600

Schmeling D, Volkmann A, 2020. On the experimental investigation of novel low-momentum ventilation concepts for cooling operation in a train compartment. *Building and Environment*, 182:107116. https://doi.org/10.1016/j.buildenv.2020.107116

Schmeling D, Kühn M, Schiepel D, et al., 2022. Analysis of aerosol spreading in a German Inter City Express (ICE) train carriage. *Building and Environment*, 222:109363. https://doi.org/10.1016/j.buildenv.2022.109363

Schwarz WH, Cosart WP, 1961. The two-dimensional turbulent wall-jet. *Journal of Fluid Mechanics*, 10(4):481-495. https://doi.org/10.1017/S0022112061000299

Song YD, Zou YP, Yao Y, et al., 2025. Aerodynamics and countermeasures of train-tail swaying inside single-line tunnels. *Journal of Zhejiang University-SCIENCE A*, 26(5):438-455. https://doi.org/10.1631/jzus.A2400039

Suresh PR, Srinivasan K, Sundararajan T, et al., 2008. Reynolds number dependence of plane jet development in the transitional regime. *Physics of Fluids*, 20(4):044105. https://doi.org/10.1063/1.2904994

Tian HQ, 2019. Review of research on high-speed railway aerodynamics in China. *Transportation Safety and Environment*, 1(1):1-21. https://doi.org/10.1093/tse/tdz014

Triboix A, Marchal D, 2002. Stability analysis of the mechanism of jet attachment to walls. *International Journal of Heat and Mass Transfer*, 45(13):2769-2775. https://doi.org/10.1016/S0017-9310(02)00008-X

Verhoff A, 1963. The Two-Dimensional Turbulent Wall Jet with and Without an External Stream. Report 626, Princeton University, Princeton, USA.

Wang HL, Bi HQ, Zhou YL, et al., 2020. Field measurements and numerical analysis of the energy consumption of urban rail vehicle air-conditioning systems. *Applied Thermal Engineering*, 177:115497. https://doi.org/10.1016/j.applthermaleng.2020.115497

Wang J, Deng E, Ni YQ, et al., 2024. Mitigating inflow acceleration effects in twin mountains using air jets: emphasis on anti-wind for high-speed railways. *Physics of Fluids*, 36(5):055128. https://doi.org/10.1063/5.0202419

Wang TT, Zhao KH, Lu YB, et al., 2024a. The airflow characteristics and thermal comfort evaluation in high-speed train cabin with mixing ventilation: an experimental and numerical study. *Building and Environment*, 250:111187. https://doi.org/10.1016/j.buildenv.2024.111187

Wang TT, Zheng YX, Lu YB, et al., 2024b. Reducing the contaminant dispersion and infection risks in the train cabins by adjusting the inlet turbulence intensity: a study based on turbulence simulation. *Science of the Total Environment*, 930:172735. https://doi.org/10.1016/j.scitotenv.2024.172735

Woodward H, de Kreij RJB, Kruger ES, et al., 2022. An evaluation of the risk of airborne transmission of COVID-19 on an inter-city train carriage. *Indoor Air*, 32(10):e13121. https://doi.org/10.1111/INA.13121

Wu F, Dong H, Yu C, et al., 2024. Numerical simulation of formaldehyde distribution characteristics in the high-speed train cabin. *Building Simulation*, 17(2):285-300. https://doi.org/10.1007/s12273-023-1078-1

Wu SB, Li T, Zhang JY, 2023. Effect of combined side-wall air supply on ventilation and respiratory pollutant dispersion

characteristics of high-speed trains. *Engineering Applications of Computational Fluid Mechanics*, 17(1):2272646. https://doi.org/10.1080/19942060.2023.2272646

Wu SB, Li T, Zhang JY, 2025. Flow field characteristics in high-speed train cabin: negative effect of non-vertical air supply. *Journal of Central South University*, 32(8):3173-3186. https://doi.org/10.1007/s11771-025-6019-y

Xu RZ, Wu F, Li XL, et al., 2022. Numerical comparison of ventilation modes on the transmission of coughing droplets in a train compartment. *Journal of Wind Engineering and Industrial Aerodynamics*, 231:105240. https://doi.org/10.1016/j.jweia.2022.105240

Xu RZ, Wu F, Pan XW, et al., 2026. A novel prediction framework for long-term aerosol dynamics and infection risk assessment in high-speed train cabins. *Building and Environment*, 288:114010. https://doi.org/10.1016/j.buildenv.2025.114010

Yang L, Li MX, Li XD, et al., 2018. The effects of diffuser type on thermal flow and contaminant transport in high-speed train (HST) cabins–a numerical study. *International Journal of Ventilation*, 17(1):48-62. https://doi.org/10.1080/14733315.2017.1351736

Yang WC, Wang J, Deng E, et al., 2024. A hybrid ventilation scheme applied to bidirectional excavation tunnel construction with a long inclined shaft. *Journal of Central South University*, 31(9):3187-3205. https://doi.org/10.1007/s11771-024-5732-2

Yin HG, Huo YK, Wang YY, et al., 2021. Numerical investigation on mechanisms and performance of column attachment ventilation for winter heating. *Building and Environment*, 202:108025. https://doi.org/10.1016/j.buildenv.2021.108025

Yu H, Liao CM, Liang HM, 2003. Scale model study of airflow performance in a ceiling slot-ventilated enclosure: isothermal condition. *Building and Environment*, 38(11):1271-1279. https://doi.org/10.1016/S0360-1323(03)00131-8

Zhang JL, Li XM, Zhao TY, et al., 2015. Experimental study on a novel fuzzy control method for static pressure reset based on the maximum damper position feedback. *Energy and Buildings*, 108:215-222. https://doi.org/10.1016/j.enbuild.2015.09.014

Zhang L, Dai ZY, Li T, et al., 2022. Multi-objective aerodynamic shape optimization of a streamlined high-speed train using Kriging model. *Journal of Zhejiang University-SCIENCE A*, 23(3):225-242. https://doi.org/10.1631/jzus.A2100329

Electronic supplementary materials

Sections S1–S4